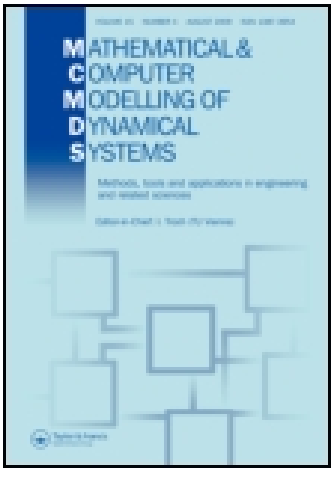

Mathematical and Computer Modelling of Dynamical Systems: Methods, Tools and Applications in Engineering and Related Sciences

Publication details, including instructions for authors and subscription information:
http://www.tandfonline.com/loi/nmcm20

Lattice Boltzmann method as a computational framework for multiscale haemodynamics

Giuseppe Pontrelli[a], Ian Halliday[b], Simone Melchionna[c], Tim J. Spencer[b] & Sauro Succi[a]

[a] Istituto per le Applicazioni del Calcolo-Consiglio Nazionale delle Ricerche (IAC-CNR), Rome, Italy

[b] MERI, Sheffield Hallam University, Sheffield, UK

[c] Istituto per i Processi Chimico-Fisici-Consiglio Nazionale delle Ricerche (IPCF-CNR), Rome, Italy

Published online: 09 Sep 2013.

To cite this article: Giuseppe Pontrelli, Ian Halliday, Simone Melchionna, Tim J. Spencer & Sauro Succi (2014) Lattice Boltzmann method as a computational framework for multiscale haemodynamics, Mathematical and Computer Modelling of Dynamical Systems: Methods, Tools and Applications in Engineering and Related Sciences, 20:5, 470-490, DOI: 10.1080/13873954.2013.833523

To link to this article: http://dx.doi.org/10.1080/13873954.2013.833523

Mathematical and Computer Modelling of Dynamical Systems, 2014
Vol. 20, No. 5, 470–490, http://dx.doi.org/10.1080/13873954.2013.833523

Lattice Boltzmann method as a computational framework for multiscale haemodynamics

Giuseppe Pontrelli[a]*, Ian Halliday[b], Simone Melchionna[c], Tim J. Spencer[b] and Sauro Succi[a]

[a]*Istituto per le Applicazioni del Calcolo-Consiglio Nazionale delle Ricerche (IAC–CNR), Rome, Italy;* [b]*MERI, Sheffield Hallam University, Sheffield, UK;* [c]*Istituto per i Processi Chimico-Fisici-Consiglio Nazionale delle Ricerche (IPCF–CNR), Rome, Italy*

(*Received 14 September 2012; final version received 7 August 2013*)

Recent developments of the lattice Boltzmann method for large-scale haemodynamic applications are presented, with special focus on multiscale aspects, including the self-consistent dynamics of suspended biological bodies and their coupling to surface structures, such as the glycocalyx, in the proximity of endothelium using unstructured grids. The description of such multiscale phenomena, each one treated with a suitable variation of the lattice Boltzmann method, opens up new perspectives for a fundamental understanding of the physical mechanisms underlying cardiovascular pathologies, such as plaque growth and the subsequent development of atherosclerotic diseases.

Keywords: haemodynamics; red blood cells; glycocalyx; wall shear stress; lattice Boltzmann method

1. Introduction

A deeper understanding of the physical mechanisms underlying the correct functioning of the human body, from the cellular to the organ level, stands out as one of the major challenges in modern science. The ultimate goal is to turn heuristic knowledge into predictive capabilities, based on quantitative modelling of the fundamental interactions between basic biochemical processes and their mechanical-hydrodynamic environment. The range of space-time scales involved in the process is daunting, from nanometres at the molecular level, all the way up, to the size of the human body, i.e. nine orders of magnitude, and more than twice as much in time, from femtoseconds of chemical bond formation to the multi-year development of diseases. Taking such daunting spectrum of scales in a single modelling swoop is utterly unfeasible and, in many respects, undesirable as well, since the amount of information involved is overwhelming to the point of obscuring the task of extracting knowledge from information. A much more sensible procedure is to take advantage of the hierarchical structure of the human body and focus the modelling effort on treatable subsets – let's name them *compartments* – of the full system (the time-honoured roman principle *divide et impera*) and patch them together at the end of the process. This entails two concurrent and cooperative functional tasks: a sharp-shooted modelling focus

*Corresponding author. Email: giuseppe.pontrelli@gmail.com

on the basic physics of each compartment and a system-engineering (system-biology, in fact) approach to glue back the various compartments together into a unified full-scale picture. None of the two can afford the luxury of exact solutions, but each has to proceed instead through a sequence of progressive refinements, until a satisfactory solution is attained. Thanks to the development of computing power and the concurrent progress in numerical techniques, especially for parallel computers, the aforementioned multiscale strategy has resulted in major breakthroughs in many areas of biology and quantitative medicine [1]. In this paper, we shall be dealing with multiscale modelling techniques for a major compartment of the human body, the cardiovascular system.

The cardiovascular system is a complex adaptive network including centimetre-sized vessels, like the aorta, down to micrometric capillaries. The study of blood flow in the large vessels has been the object of computational studies for several decades now, and it is fair to say that computational haemodynamics (CHD) is now in a position to provide a very accurate information of the blood flow structure, even in anatomically realistic geometries. On the other hand, traditional CHD is designed to discard microscopic details, such as the granular nature of blood (a suspension of red and white blood cells, platelets and other microscopic biological bodies), which may play a major role in shaping the interaction with endothelial cells and the ensuing build-up of the biochemical response of the cellular tissue, with far-reaching implications for the long-term development of cardiovascular conditions. The study of blood in the macrovasculature, as much as in capillaries, has deep implications for the understanding and prevention of the most common cardiovascular pathologies, atherosclerosis being possibly the most outstanding example in point. The build-up of the resultant soft tissue and the eventual changes in its consistency leads to serious atherosclerotic pathologies, including catastrophic events such as plaque rupture [2]. Atherosclerotic plaques appear in regions of disturbed blood flow where the local wall shear stress (WSS) is low (<1.0 Pa) or of alternating direction [3]. Hence, plaques tend to form near arterial bifurcations where the flow is always altered compared to unbranched regions [4].

Atherosclerosis primarily affects the coronary arteries and the evidence that low average WSS has a key role in the disease localization and progression is widely accepted [5–7]. Predictions of where and how the illness is likely to develop can be obtained by using fluid dynamics simulations as a routine methodology to study blood flow patterns in human arteries. As a matter of fact, the shape and the structure of endothelium plays a number of important roles in the vascular system, and its dysfunction may lead to several pathological states, including early development of atherosclerosis [8]. The microscopic shape of the endothelium is defined by the presence of endothelial cells (ECs henceforth), making the arterial wall undulated. This effect becomes more pronounced in small-sized vessels, where the corrugation degree increases. The study of blood flow over a regularly undulating wall made of equally aligned and distributed ECs has been recently carried out in [9], where the variation of WSS over the ECs has been computed. Furthermore, the endothelium is coated by long-chained macromolecules and proteins which form a thin porous layer, called the glycocalyx [10]. The glycocalyx has a *brushlike* structure and a thickness which varies with the vessel diameter, but its average is 100 nm for arterioles. It has several roles: it serves as a transport barrier to prevent ballistic red blood cell interactions with the endothelium and as a sensor and a transducer of mechanical forces, such as fluid shear stress, to the surface of ECs. Actually, it has been recognized that the glycocalyx responds to the flow environment and, in particular, to the fluid stress, but the mechanism by which these proteins sense the shearing forces and transduce mechanical into biochemical signals is still not fully understood [8]. The glycocalyx itself is remodelled by the shearing flow and by the compression exerted by the deformed erythrocytes in capillaries [11].

Flow-induced mechano-transduction in ECs has been studied over the years with emphasis on correlation between disturbed flow and atherosclerosis. Recently, some mathematical modelling work has been carried out, using a porous medium to model the endothelial surface layer (ESL henceforth) [12,13]. However, none of these works include the effect of the roughness of the wall, which should be incorporated for a more realistic description at the microscopic level. The importance of treating blood as a suspension of erytrocytes or red blood cells (RBCs) in the plasma has been addressed by many authors, who developed a number of analyses to model single RBC in microvessels with complex boundary shapes and interactions by deformable vesicles [2,11].

In the following sections, we will present a coarse-grained model that attempts to include some of the basic physical microscale effects of the ESL attached to the ECs exploring to what extent the WSS may vary due to this layer, in addition to the previously examined EC shape and particulate transport [9].

One of the direct benefits of the joint use of simulation and imaging techniques is to understand the connection between fluid-mechanical flow patterns and plaque formation and evolution. This has important implications for predicting the course of atherosclerosis and possibly preventing or mitigating its effects, in particular, by non-invasively and inexpensively screening large numbers of patients for incipient arterial disease and to intervene at clinical level prior to the occurrence of a catastrophic event. One option is to obtain the arterial wall shape, plaque morphology and lumen anatomy from the non-invasive multi-detector computed tomography (MDCT) imaging technique, as in the newest systems with 320-detector rows, a technology that enables three-dimensional Cartesian acquisition of the entire arterial tree in a single heart beat and provides high accuracy of nominal resolution of 0.1 mm [14].

The lattice Boltzmann (LB) method is particularly suitable for handling such complex arterial geometries, since most of its simplicity stems from an underlying Cartesian mesh over which fluid motion is represented. LB is based on moving information along straight-line trajectories, associated with the constant speed of fictitious molecules which characterize the state of the fluid at any instant and spatial location. This picture stands in sharp contrast with the fluid dynamics representation, in which, by definition, information moves along the material lines defined by fluid velocity itself, usually a very complex space-time dependent vector field. This main asset has motivated the increasing use, over the last decade, of LB techniques for a variety of biological processes [15] and multiscale physical systems [16], including CHD [17–20].

Simulations of blood flows based on the LB method provide a particularly efficient and flexible framework in handling complex arterial geometries. In the past, the LB method has been applied to a broad range of fluid dynamics problems, including turbulence and multiphase flows [21], as well as in blood flow simulations in steady and pulsatile regimes and with non-Newtonian flows through stenoses [22].

The main aim of this paper is to show that the LB method provides an encompassing analytical/computational framework embedding microscopic effects, namely RBCs, endothelial corrugations and glycocalyx structures, within a continuum haemodynamic description. It is here demonstrated its capability of spanning a range of two- and three-dimensional models and scales relevant to blood flow [18,23].

The possibility of embedding suspended bodies in the surrounding plasma and the glycocalyx representation over an undulated endothelial wall addresses two major steps forward in the modelling of blood from a bottom-up perspective. This would permit to check the validity of the many assumptions that continuum haemodynamics is based upon, discarding those which do not match the microscopic description and possibly improving on those which do only in part.

2. The lattice Boltzmann method for continuum haemodynamics

In the last decade, the LB method has captured increasing attention from the fluid dynamics community as a competitive computational alternative to the discretization of the Navier–Stokes equations of continuum mechanics. LB is a hydrokinetic approach and a minimal form of the Boltzmann kinetic equation, based on the collective dynamics of fictitious particles on the nodes of a regular lattice. The dynamics of fluid particles is designed in such a way as to obey the basic conservation laws ensuring hydrodynamic behaviour in the continuum limit, in which the molecular mean free path is much shorter than typical macroscopic scales [21]. This condition is clearly met in most blood flow regimes, together with the Newtonian rheological behaviour of blood in large arterial systems. Non-Newtonian rheological models appropriate for simulating blood flow in medium or small-sized arteries, such as the Casson, Carreau or Carreau-Yasuda models, can also be incorporated within the LB approach [24,25].

The LB method can be regarded as a mesoscopic (between microscopic and macroscopic) approach for modelling macroscopic hydrodynamics. Rather than following the position and velocity of each particle in the system, as is done in microscopic models (i.e. molecular dynamics), the fluid flow is described by tracking the evolution of the density distribution function (or population). In other words, the LB method is based on the collective dynamics of fictitious particles on the nodes of a regular lattice where the basic quantity is $f_p(\mathbf{x}, t)$, representing the probability of finding a 'fluid particle p' at the mesh location $\mathbf{x}$ and at time t and travelling with discrete speed $\mathbf{c}_p$. 'Fluid particles' represent the collective motion of a group of physical particles.

The rate of change of the single-particle distribution function is given by the following discrete Boltzmann equation:

$$\partial_t f_p + \mathbf{c}_p \cdot \nabla f_p = -\frac{1}{\tau}\left(f_p - f_p^{\mathrm{eq}}\right) \tag{1}$$

where the left-hand side represents the molecular free streaming, whereas the right-hand side represents molecular collisions via a single-time relaxation towards local equilibrium f_p^{eq} on a typical timescale τ [21]. The latter is called the relaxation time and, in macroscopic terms, is related to the fluid viscosity.

To discretize the previous equation, we employ the common three-dimensional 19-speed cubic lattice (D3Q19) with mesh spacing Δx, where the discrete velocities $\mathbf{c}_p$ connect mesh points to first and second neighbours (Figure 1) [26].

The fluid populations are advanced in a timestep $\Delta t = 1$ through the following evolution equation:

$$f_p(\mathbf{x} + \mathbf{c}_p \Delta t, t + \Delta t) = f_p(\mathbf{x}, t) - \omega(f_p - f_p^{\mathrm{eq}})(\mathbf{x}, t) + F_p(\mathbf{x}, t) \tag{2}$$

The right-hand side of Equation (2) represents the effect of fluid-fluid molecular collisions, through a relaxation towards a local equilibrium, typically a second-order expansion in the fluid velocity of a local Maxwellian with velocity $\mathbf{u}$,

$$f_p^{\mathrm{eq}} = w_p \rho \left[1 + \frac{\mathbf{u} \cdot \mathbf{c}_p}{c_s^2} + \frac{\mathbf{u}\mathbf{u} : (\mathbf{c}_p \mathbf{c}_p - c_s^2 \mathbf{I})}{2c_s^4}\right] \tag{3}$$

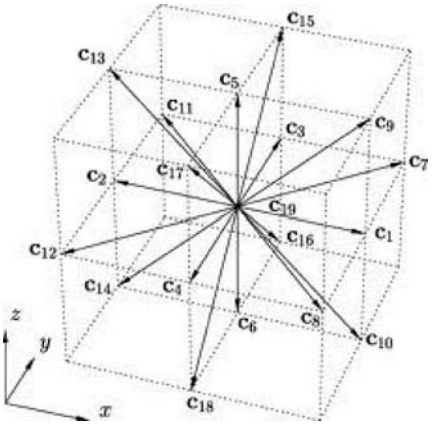

Figure 1. The D3Q19 cubic lattice.

where $c_s = 1/\sqrt{3}$ is the speed of sound, w_p is a set of weights normalized to unity and $\mathbf{I}$ is the unit tensor in Cartesian space. The relaxation frequency $\omega = \frac{1}{\tau}$ controls the kinematic viscosity of the fluid. The kinetic moments of the discrete populations provide the local mass density $\rho(\mathbf{x}, t) = \sum_p f_p(\mathbf{x}, t)$ and momentum $\rho\mathbf{u}(\mathbf{x}, t) = \sum_p \mathbf{c}_p f_p(\mathbf{x}, t)$. The last term F_p in Equation (2) represents a momentum source, given by the presence of suspended bodies, if RBCs are included in the model, as discussed in the following sections. Through the Chapman–Enskog procedure, in the incompressible limit, the Navier–Stokes equations:

$$\nabla \cdot \mathbf{u} = 0$$

$$\frac{\partial \mathbf{u}}{\partial t} + (\mathbf{u} \cdot \nabla)\mathbf{u} = -\frac{1}{\rho}\nabla P + \nu\nabla^2\mathbf{u} + \mathbf{F} \tag{4}$$

are recovered from Equation (2) [21], where P is the pressure, $\nu = c_s^2 \Delta t \left(\frac{1}{\omega} - \frac{1}{2}\right)$, the kinematic viscosity, and $\mathbf{F}$ is any body force, corresponding to F_p in Equation (2).

The LB is a low-Mach, weakly compressible fluid solver and presents several major advantages for the practical implementation in complex geometries. In particular, in CHD, the curved blood vessels are shaped on the Cartesian mesh scheme via a staircase representation, in contrast to body-fitted grids that can be employed in direct Navier–Stokes simulations. This apparently crude representation of the vessel walls is sufficient at macroscopic level and can be systematically improved by increasing the mesh resolution.

LB allows to impose no-slip boundary conditions at the endothelium by employing the bounce-back method; this consists of reversing at every timestep the post-collisional populations pointing towards a wall node, providing first-order accuracy for irregular walls [21]. In the bounce-back method, the points corresponding to the exact no-slip hydrodynamic surface fall at intermediate positions between the external fluid mesh nodes and the nearby wall mesh nodes. Owing to its simplicity, the method handles irregular vessel boundaries by a linear interpolation maintaining first-order accuracy. More sophisticated alternatives with higher-order accuracy are available [27–29].

The WSS, which is a crucial quantity in haemodynamic applications, can be computed via the deviatoric stress tensor $\sigma(\mathbf{x}, t) \equiv \nu\rho\left(\partial_{\mathbf{x}}\mathbf{u} + \partial_{\mathbf{x}}\mathbf{u}^T\right)$ and evaluated via its kinetic representation:

$$\sigma(\mathbf{x},t) = -\frac{\nu\omega}{c_s^2}\sum_p \mathbf{c}_p\mathbf{c}_p(f_p - f_p^{\mathrm{eq}})(\mathbf{x},t) \tag{5}$$

The second tensor invariant is the wall shear stress or WSS,

$$\mathcal{S}(\mathbf{x}_w,t) = \sqrt{\frac{1}{2}(\sigma:\sigma)(\mathbf{x}_w,t)} \tag{6}$$

where $\mathbf{x}_w$ represents the position of sampling points in close proximity to the mesh wall nodes. $\mathcal{S}(\mathbf{x}_w,t)$ provides a direct measure of the strength of the near-WSS [30]. It is worth mentioning that the WSS evaluation via Equation (5) and (6) is completely local and does not require any finite-differencing procedure. This is particularly advantageous near boundaries where the computation of gradients is very sensitive to morphological details. Moreover, Equation (5) and (6) are usually second-order accurate on the standard LB, but degrade to first order in the case of irregular wall shapes [27,31]. Further theoretical and algorithmic details about the accuracy of WSS in such cases can be found in [32,33]. In order to sample high signal/noise WSS data, the LB mesh needs high spatial resolution, with mesh spacing being as small as $\Delta x \simeq 50\,\mu$m for standard fluid dynamic simulations, or being as small as $\Delta x \simeq 10\,\mu$m in order to account for the presence of RBCs. Simulations in extended arterial systems are based on the acquisition of MDCT data which are segmented into a stack of slices, followed by a mesh generation from the segmented slices. For a typical coronary artery system, the procedure to build the LB mesh from the MDCT raw data starts from a single vessel, formatted as stacked bi-dimensional contours (slices), with a nominal resolution of 100 μm. In spite of recent technological progress, this resolution is still insufficient and the inherently noisy geometrical data pose a problem in the evaluation of WSS, a quantity that proves extremely sensitive to the details of the wall morphology. Thus, raw MDCT data present a mild level of geometric irregularities that can affect the quality of the LB simulations. For the simulation, we resort to regularize the initial geometry by smoothing the sequence of surface points via a linear filter along the longitudinal direction. Similarly, one could filter out surface points along the azimuthal contour. We have shown that such smoothing is necessary in order to avoid strong artefacts in the simulation results [34]. Even if the precise shape of the vessel is unknown, as it falls within the instrumental indeterminacy, the numerical results converge to a common fluid dynamic pattern as the smoothing procedure reaches a given level. The regularized geometries are still of great interest because they obey the clinical perception of a smooth arterial system and, moreover, the smoothing procedure falls within the intrinsic flexibility of the arterial system.

When studying coronary arteries as a prototypical system for plaque formation and development, one issue regards the presence of deformable vessels. Whereas larger arteries undergo high deformations, a simple calculation shows that the distensibility index of a coronary artery of sectional area A is $b^{-1} \simeq 1.5$ mm Hg. Therefore, the arterial section during a heartbeat has a maximal deformation of $\delta A/A = b\Delta P$, where ΔP is the maximal pressure variation over a cardiac cycle. For a pressure jump of 40 mm Hg, the deformation is less than 3% and thus modelling the coronary system as rigid does not introduce major artefacts in the computed flow and pressure distributions.

In a branched portion of arteries, boundary conditions at the inlet and multiple outlets can be chosen in different ways, typically by following the flow–pressure, pressure–pressure or flow–flow prescriptions. The first two options are more popular in fluid dynamic models, and pressure conditions at the outlets reflect the presence of a recipient medium.

Even flow–flow conditions have found some applicability, as they can accommodate some type of metabolic autoregulation as encoded by Murray's law [35]. It is worth mentioning that flow–flow conditions can give rise to numerical instabilities in simple pipe flows, as long-living transients can develop. The absence of a peripheral system can be compensated by using an equivalent RCL circuit at each system outlet, where the auxiliary circuitry introduces an external viscous dissipation (R), vessel compliance (C) and fluid inertia (L) and compensates for the missing components (lumped parameter model).

In the framework of the LB method, boundary conditions at the inlet and multiple outlets can be imposed as follows. A constant velocity (with plug or parabolic profile) is enforced at the entrance of the main artery, as a way to control the amplitude of the flow. Even if the inlet profiles are not the real ones for irregular geometries, they fulfil the purpose of imposing the total flow rate in the chosen region. The fluid flow spontaneously and rapidly develops the consistent profile already at a short distance downstream. A constant pressure is imposed on the several outlets of the main artery, as well as on the outlet of all secondary branches (of the order of 10 in typical coronary systems). This leaves the simulation with the freedom of creating an appropriate velocity profile in the outlet regions and building up a pressure drop between the inlet and several outlets. The Zou–He method [36] is used to implement both the velocity inlet and the pressure outlets. This method exploits information streamed from fluid bulk nodes onto boundary cells and imposes a completion scheme for particle populations which are unknown because their neighbouring nodes are not part of the fluid domain. The boundary cells are treated as normal fluid cells where the conventional LB scheme holds. Thanks to this natural integration of the boundary scheme, the method is second-order accurate in space, compatible with the overall accuracy of the LB method [37]. The method handles in a natural way time-dependent inflow conditions for pulsatile flows. The algorithm requires that all nodes of a given inlet or outlet are aligned on a plane which is perpendicular to one of the three main axes, although the injected flow profile and direction can be arbitrary. However, since the inlet section is typically a critical region of simulation in terms of numerical stability due to the high fluid velocities, it is preferable to have an incoming flow direction aligned with one the Cartesian axis. This requirement can be fulfilled by rotating the artery in such a way as to align the inlet axis with one of the Cartesian axis, which guarantees an exact control on the flow imposed at the inlet. Conversely, the outlet planes are not, in general, normal to the orientation of the blood vessels. However, this does not lead to noticeable problems because the pressure drop along typical arterial systems is mild and the error due to imposing a constant pressure along an inclined plane is negligible. Although our model is restricted to a particular case, other alternative approaches for the treatment of more general outflow conditions are available [38].

3. Modelling blood as a suspension

Blood is a complex fluid made of many corpuscular elements suspended in the plasma. RBCs constitute an important component in blood because of their large number and their crucial role in oxygen transport. Typically, a human RBC has a biconcave shape with $\sim 8\ \mu$m diameter and $\sim 2\ \mu$m thickness. The interior fluid has a viscosity of $6\,cP$, which is about five times of that of the suspending plasma. The cell membrane is highly deformable, so the RBCs can pass through capillaries of as small as 4 μm inner diameter with large deformation; they exhibit both rotational and orientational responses that effect and modulate blood rheology [2]. While blood flow is quasi-Newtonian away from the endothelial region, the presence of RBCs strongly affects flow in the proximity of the endothelium,

where the interplay of RBC crowding for haematocrit levels up to 50%, depletion due to hydrodynamic forces and RBCs' arrangement in rouleaux takes place.

In order to consider these different factors, we have recently proposed a model that focuses on three independent components: the far-field hydrodynamic interaction of an RBC in a plasma solvent, the raise of viscosity of the suspension with the hematocrit level and the many-body collisional contributions to viscosity [39]. These three critical components conspire to produce large-scale haemorheology and the local structuring of RBCs. The underlying idea is to represent the different responses of the suspended bodies, emerging from the rigid body as much as the vesicular nature of the globule, by distinct coupling mechanisms. These mechanisms are entirely handled at kinetic level, that is, the dynamics of plasma and RBCs is governed by appropriate collisional terms that avoid to compute hydrodynamic forces and torques via the Green's function method, as employed in Stokesian dynamics [40]. The fundamental advantage of hydrokinetic modelling is to avoid such an expensive route and, at the same time, enabling to handle finite Reynolds conditions and complex or irregular boundaries within the simple collisional approach. At the macroscopic scale, the non-trivial rheological response emerges spontaneously as a result of the underlying microdynamics.

In our modelling approach, an RBC is introduced as a body having position $\mathbf{R}_i$, velocity $\mathbf{V}_i$, angular velocity $\mathbf{\Omega}_i$ and instantaneous orientation given by the matrix

$$\mathbf{Q}_i = \begin{pmatrix} n_{x,i} & t_{x,i} & g_{x,i} \\ n_{y,i} & t_{y,i} & g_{y,i} \\ n_{z,i} & t_{z,i} & g_{z,i} \end{pmatrix} \tag{7}$$

and where $\mathbf{n}_i$, $\mathbf{t}_i$ and $\mathbf{g}_i$ are orthogonal unit vectors, such that $\mathbf{Q}_i^T \mathbf{Q}_i = \mathbf{1}$. We introduce a function to account for the ellipsoidal shape and orientation via the following expression:

$$\tilde{\delta}(\mathbf{x}, \mathbf{Q}_i) \equiv \prod_{\alpha=x,y,z} \tilde{\delta}_\alpha[(\mathbf{Q}_i \mathbf{x})_\alpha] \tag{8}$$

with

$$\tilde{\delta}_\alpha(\tilde{y}_\alpha) \equiv \begin{cases} \dfrac{1}{8}\left(5 - 4|\tilde{y}_\alpha| - \sqrt{1 + 8|\tilde{y}_\alpha| - 16\tilde{y}_\alpha^2}\right) & |\tilde{y}_\alpha| \le 0.5 \\ \dfrac{1}{8}\left(3 - 4|\tilde{y}_\alpha| - \sqrt{-7 + 24|\tilde{y}_\alpha| - 16\tilde{y}_\alpha^2}\right) & 0.5 < |\tilde{y}_\alpha| \le 1 \\ 0 & |\tilde{y}_\alpha| > 1 \end{cases}$$

and $\tilde{y}_\alpha \equiv (\mathbf{Q}_i \mathbf{x})_\alpha / \xi_\alpha$ and ξ_α being a set of three integers for each Cartesian component $\alpha = x, y, z$, representing the ellipsoidal radii in the three principal directions [39].

The RBC-fluid translational coupling is given by the following kernel:

$$\boldsymbol{\phi}(\mathbf{x}, i) = -\gamma_T \tilde{\delta}_i \, (\mathbf{V}_i - \mathbf{u}) \tag{9}$$

where γ_T is a translational coupling coefficient and $\tilde{\delta}_i \equiv \tilde{\delta}(\mathbf{x} - \mathbf{R}_i, \mathbf{Q}_i)$ is a short-hand notation.

The RBC-fluid rotational coupling has different origins. By considering the general decomposition of the deformation tensor in terms of purely elongational and rotational

terms $\partial \mathbf{u} = \mathbf{e} + \boldsymbol{\rho}$, where $\mathbf{e} = \frac{1}{2}(\partial \mathbf{u} + \partial \mathbf{u}^T)$ is the rate of strain tensor and $\boldsymbol{\rho} = \frac{1}{2}(\partial \mathbf{u} - \partial \mathbf{u}^T)$ is the vorticity tensor, the rotational component of the deformation tensor generates solid-like tumbling motion, while the rotational and elongational terms generate tank-treading motion [39]. Consequently, at rotational level, RBC experiences two distinct torques: (1) the coupling between the body motion and the fluid vorticity, given by the kernel

$$\boldsymbol{\tau}^A(\mathbf{x}, i) = -\gamma_R \tilde{\delta}_i \, (\boldsymbol{\Omega}_i - \boldsymbol{\omega}) \tag{10}$$

where γ_R is a coupling coefficient and (2) the elongational component of the flow contributes to the orientational torque for bodies with ellipsoidal symmetry. By defining the stress vector $\mathbf{t}^{\boldsymbol{\sigma}} = \boldsymbol{\sigma} \cdot \mathbf{n}$, where $\mathbf{n}$ is the outward normal to the surface of a macroscopic RBC, the surface normal is replaced by the vector spanning over the volume of the diffused particle, i.e. $\mathbf{n} = \partial \tilde{\delta} / |\partial \tilde{\delta}|$. The associated torque is given by

$$\boldsymbol{\tau}^S(\mathbf{x}, i) = \chi \tilde{\delta}_i \mathbf{t}^{\boldsymbol{\sigma}} \times (\mathbf{x} - \mathbf{R}_i) \tag{11}$$

where χ is a control parameter.

Finally, the elongational torque includes an independent contribution arising from tank treading based on the vesicular nature of the RBC. Its effect is included by considering that tank-treading couples to both the rotational and elongational flow components and results in a net torque with the same angular symmetry of the tumbling response. Thus, the extent of tank-treading response is controlled by the intensity of the elongational torque, that is by choosing an appropriate value for α [39].

Once the roto-translational coupling kernels have been introduced, the hydrodynamic force and torque acting on the RBC are obtained via integration over the globule spatial extension. Owing to the discrete nature of the mesh, the coupling kernels are expressed as discrete sums:

$$\mathbf{D}_i = \sum_{\mathbf{x}} \boldsymbol{\phi}(\mathbf{x}, i) \tag{12}$$

$$\mathbf{T}_i = \sum_{\mathbf{x}} \boldsymbol{\tau}^A(\mathbf{x}, i) + \boldsymbol{\tau}^S(\mathbf{x}, i) \tag{13}$$

Forces and torques act on the fluid according to the term

$$\mathbf{G} = -\sum_i \left\{ \mathbf{D}_i \tilde{\boldsymbol{\delta}}_i + \frac{1}{2} \mathbf{T}_i \times \partial \tilde{\delta}_i \right\}$$

Some algebra shows that the action of the forces $\mathbf{D}_i$ and torques $\mathbf{T}_i$ are counterbalanced by opposite reactions on the fluid side. Conservation of linear and angular momentum in the fluid-RBC system preserves the basic symmetries of the microdynamics and produces consistent hydrodynamic response.

The explicit force exerted by the RBCs on the fluid is given by the term (see Equation (2)):

$$F_p = w_p \left[\frac{\mathbf{G} \cdot \mathbf{c}_p}{c_s^2} + \frac{(\mathbf{G} \cdot \mathbf{c}_p)(\mathbf{u} \cdot \mathbf{c}_p) - c_s^2 \mathbf{G} \cdot \mathbf{u}}{c_s^4} \right] \tag{14}$$

Within the LB scheme, this equation produces first-order accurate body forces. Higher order methods such as those described in [41], could be adopted. However, given the non-trivial dependence of the forces/torques on the fluid velocity/vorticity, Guo's method would require an implicit numerical scheme, whereas it is preferable to employ an explicit, first-order accurate scheme.

RBCs are carriers of an internal fluid that contributes significantly to the dissipation of energy. The consequence of which is the rapid growth of the apparent viscosity with the haematocrit level. The effect of the inner fluid is considered by locally enhancing the LB fluid viscosity within the RBC extension. In the LB scheme, this is easily accomplished by the following relaxation time:

$$\tau(x) = \tau_0 + \Delta \sum_i \tilde{\theta}_i \tag{15}$$

where τ_0 corresponds to the viscosity of pure plasma, Δ is viscosity enhancement factor and $\tilde{\theta}_i$ is the ellipsoidal characteristic function, related to $\tilde{\delta}$ in Equation (8). By choosing $\nu_0 = 1/6$ and $\Delta = 2$, the ratio between inner ($\tilde{\theta}_i \sim 1$) and outer ($\tilde{\theta}_i \sim 0$) viscosities corresponds to the physiological value of 5.

Besides hydrodynamic interactions, mechanical forces regulate the packing attitude and structuring of RBCs. These interactions are modelled as pairwise forces by means of the Gay–Berne (GB) potential [42], the pairwise GB energy being a function of the relative distance and orientation between RBCs. Given the principal axes $(a_{i,1}, a_{i,2}, a_{i,3})$ of the ith globule, the ellipsoidal shape associated to the excluded volume interactions is constructed according to the shape matrix $\mathbf{S}_i = \mathrm{diag}(a_{i,1}, a_{i,2}, a_{i,3})$ and the transformed matrix $\mathbf{A}_i = \mathbf{Q}_i \mathbf{S}_i^2 \mathbf{Q}_i^T$ in the laboratory frame. The pair of particles i,j at distance $\mathbf{R}_{ij}$ experiences a characteristic exclusion distance η_{ij} that depends on the RBCs mutual distance, shape and orientation, written as

$$\eta_{ij} = \frac{1}{\sqrt{\phi_{ij}}} \qquad \phi_{ij} = \frac{1}{2} \mathbf{R}_{ij} \cdot \mathbf{Y}_{ij}^{-1} \cdot \mathbf{R}_{ij}$$

where $\mathbf{Y}_{ij} \equiv \mathbf{A}_i + \mathbf{A}_j$. A purely repulsive potential is given by [42,43]:

$$\begin{cases} 4\Sigma_0(\rho_{ij}^{-12} - \rho_{ij}^{-6}) + \Sigma_0 & \rho_{ij}^6 \leq 2 \\ 0 & \rho_{ij}^6 > 2 \end{cases} \tag{16}$$

with

$$\rho_{ij} = \frac{R_{ij} - \eta_{ij} + \eta_{ij}^{\min}}{\eta_{ij}^{\min}} \tag{17}$$

where Σ_0 is the energy scale and $\eta_{ij}^{\min}$ is a constant, both parameters being independent of the ellipsoidal mutual orientation and distance. For two identical oblate ellipsoids, $\eta_{ij}^{\min}$ corresponds to a contact distance of the two particles having face-to-face orientation. In general, by considering the minimum particle dimension $a_i^{\min} = \min(a_{i,1}, a_{i,2}, a_{i,3})$ then

$$\eta_{ij}^{\min} = \sqrt{2\left[\left(a_i^{\min}\right)^2 + \left(a_j^{\min}\right)^2\right]} \tag{18}$$

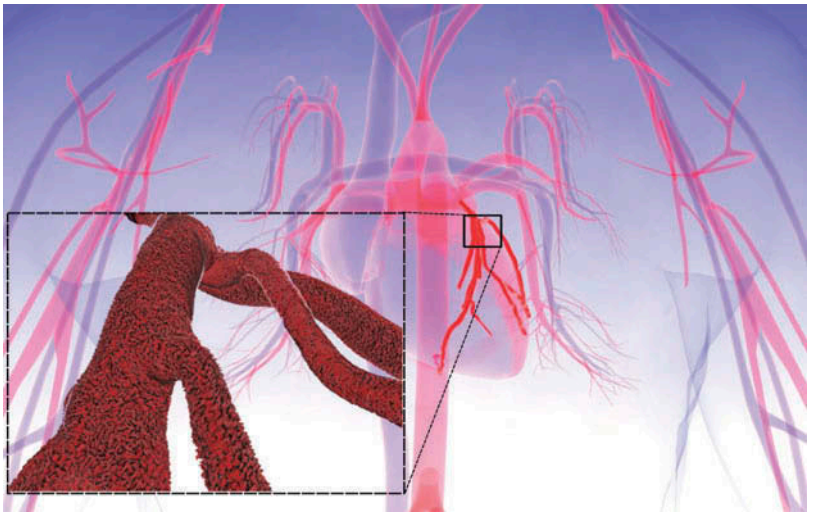

Figure 2. Schematic diagram of the circulatory system surrounding the heart. The inset illustrates a detail of the branched coronary arteries, in the presence of 50% hematocrit.

Once the forces and torques standing from both hydrodynamics and direct mechanical forces are computed, the rigid body dynamics is propagated via a time second-order accurate algorithm [44,45].

Numerical results have shown that the particulate nature of blood cannot be omitted when studying the rheology of this biofluid and the shear stress distribution in complex geometries. The model for RBCs has been tested against *in vitro* data on rheological response to data skimming and a good match has been found [39]. In addition, the pressure distribution of a complex coronary stenotic network has been compared with *in vivo* data and has been excellent agreement reported [46]. Regions of low shear stress can appear as the haematocrit reaches physiological levels as a result of the non-trivial organization of RBCs and the irregular morphology of vessels, with far reaching consequences in real-life cardiovascular applications, where the organization of RBCs impacts both the local flow patterns and the large-scale flow distribution in vascular networks [39]. A crucial advantage of the hydrokinetic model with the presence of realistic haematocrit is its reduced computational cost, thus enabling the investigation of systems of physiological relevance (Figure 2).

4. Modelling the corrugated wall surface

At a lower scale, the scale of the blood cells, new intriguing aspects come to light in haemodynamics. For example, the vessel wall surface is covered by ECs that give a wavy structure, so far neglected (Figure 3); this does not imply a significant variation in the flow field, but it can be extremely relevant in computing WSS, which is constant in a flat-walled artery. Indeed, the ECs (a single EC has been estimated to be about 15 μm long by 0.5 μm high, see [47]) form a continuous, undulated wall layer above which blood is flowing. At such mesoscopic scale, the wall may be considered as a wavy surface constituted by a regular array of equal, repeated ECs. We consider a two-dimensional channel flow between two boundary surfaces located at $y = \pm h(x)$, with the x-axis in the direction of the mean flow.

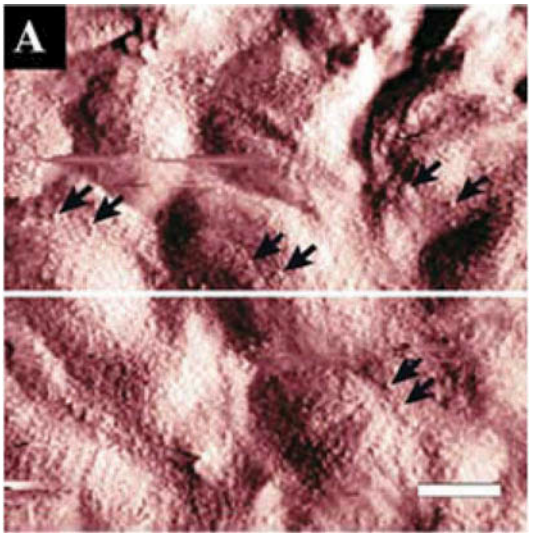

Figure 3. The rough surface of the endothelium as imaged using scanning force microscopy (from [47]). Arrows point to granular structures on ECs' surfaces, white line marks scanning line for height profile evaluation and scale bar corresponds to 5 μm.

The shape of each internal wall appears as a smoothly corrugated surface: the channel semi-width is obtained as a perturbation around a reference constant value H: $h(x) = H \pm \xi(x)$, where $\xi(x)$ is given by repeating the profile of a single EC several times and subsequently smoothing it. The quantity $\max \xi / H$ represents the corrugation degree.

For such complex geometries, the standard LB method, designed to be used over a uniform Cartesian grid, would represent a severe limitation for high resolutions near the walls. Recent advances in LB have led to a substantial enhancement for handling irregular shapes, and a particularly interesting option is represented by finite-volume formulations on fully unstructured grids [48]. The pressure-driven axi-symmetric flow of a continuum fluid through a plane channel having a corrugated surface where the grid is locally refined (Figure 4) has been recently modelled with an unstructured lattice Boltzmann equation (ULBE) in [9]. At small Reynolds number and with moderate corrugation degree, the velocity profiles preserve the parabolic shape (Figure 5). However, the wall corrugation causes a local change in the velocity derivative and hence a variation in the WSS values which match the undulation of the wall; in particular, the minimum and maximum WSS

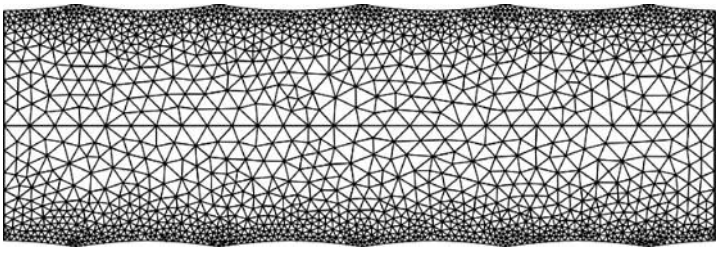

Figure 4. A two-dimensional arterial segment having a corrugated wall, covered by a near-wall refined triangular unstructured mesh.

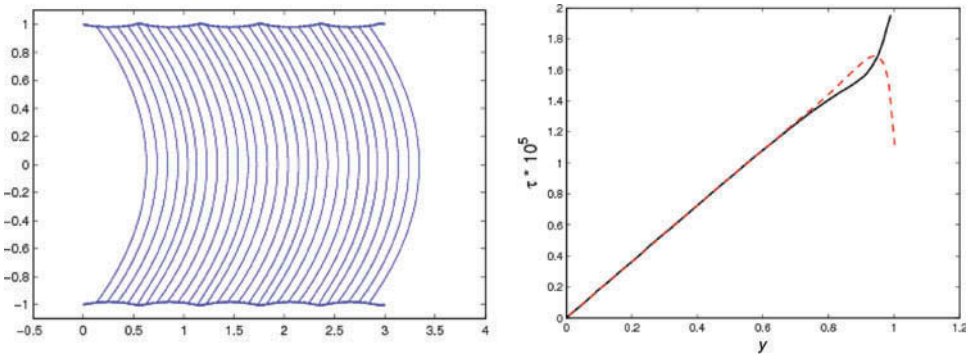

Figure 5. Parabolic velocity profiles along the wavy channel: its wall is constituted by a uniform sequence of peaks and throats (left). Cross-stream variation of shear stress in half-channel: continuous line – peak of EC; dashed line – valley of EC (LB units) (right).

values correspond to the wall throat and peak, respectively. Their values depend on the vessel diameter and on the flow rate, but their ratio remains almost constant.

As Figure 5 shows, the shear stress rises linearly in the transverse direction, except near the wall. Here, the variation in cross-sectional width generates a substantial local difference in the shear rates and stresses, and the consequence is a local variation of these quantities in a boundary layer close to the wall and an oscillation of the shear rates and WSS along the endothelium. We have further investigated the dependence and the sensitivity on the corrugation degree and quantified the WSS differences with the variation of vessel diameter and flow rates. It was shown a significant WSS variation between the wall's peaks and throats, especially in small-sized arteries [9].

5. Modelling the glycocalyx

The endothelial surface is not only wavy in its geometry but also covered by fibrous filaments and long protein chains forming a thin layer called the endothelial surface layer (ESL) or glycocalyx [10]. From a fluid dynamics point of view, the ESL can be modelled as a porous layer of constant thickness (50–100 nm), which suits the wall undulation, through which the flow of the continuous phase (plasma) is possible. This would alter the boundary condition of the problem; specifically, the classical no-slip condition at the vessel wall may have to be replaced to allow for plasma penetration through the ESL. The LB method readily accommodates a model of the glycocalyx itself, as it is particularly well suited to address what would now become a multiscale model. Furthermore, and differently than in Section 3, the mesoscopic particulate nature of the blood is now addressed in the context of a bi-component fluid model: here RBCs are deformable, neutrally buoyant liquid drops approximated by a uniform interfacial tension and suspended in the plasma. Conceptually, the idea is to solve a two-domain problem, whereby the bulk flow (in the lumen) is governed by the multicomponent Navier–Stokes equations and the near-wall region by a porous-medium Brinkmann flow formulation. At the mesoscale, the glycocalyx is not modelled in a detailed form, but its effect on the flow is still properly addressed, using methods which are amenable to coupling other, more detailed, simulations with experiments. We develop here a *two-way coupled* model where the drop interface is forced by compression of the ESL, and the effect of perturbed or compressed glycocalyx is then communicated to the flow [49]. We assume here that the filaments are strongly anchored in the endothelium,

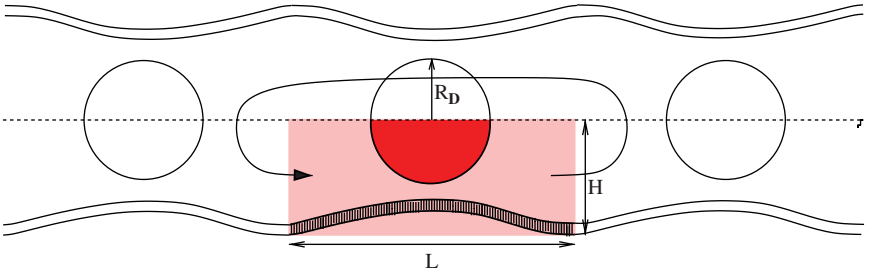

Figure 6. Schematic diagram of the model system. Exploiting axi-symmetry, flow in half-channel is considered. The hatched layer near the wall indicates the glycocalyx, and the arrow-headed line is used to point out the periodic boundary conditions at the inlet-outlet, and only the coloured portion of the vessel is considered explicitly in the simulation.

where they are most resistant to deformation, and that they deform preferably at their tip, i.e. towards the vessel lumen.

Keeping within the benefits of the LB framework, we use the mesoscale LB method to solve the governing hydrodynamic equations, which involve multi-component fluid flow, off-lattice or sub-grid, boundary surfaces and a porous-layer representative of the ESL.

We now consider a wavy two-dimensional axi-symmetric channel, having the same corrugation repeated along its length. For the sake of simplicity, a single EC is considered and periodic boundary conditions are imposed, in order to model an infinitely long channel (Figure 6). The governing hydrodynamic equations for flow in a porous medium, with constant or variable porosity ϵ, are an extension of Equation (4), as in [50]:

$$\begin{aligned} \nabla \cdot \mathbf{u} &= 0 \\ \frac{\partial \mathbf{u}}{\partial t} + (\mathbf{u} \cdot \nabla)\frac{\mathbf{u}}{\epsilon} &= \frac{1}{\rho}\nabla(\epsilon P) + \nu \nabla^2 \mathbf{u} + \mathbf{F} \end{aligned} \tag{19}$$

Here, $\mathbf{F}$ is the total body force due to the presence of both the porous material (drag) and other external forces:

$$\mathbf{F} = -\frac{\epsilon \nu}{K}\mathbf{u} - \frac{\epsilon F_\epsilon}{\sqrt{K}}\mathbf{u}|\mathbf{u}| + \epsilon \mathbf{H} \tag{20}$$

where K is the permeability, F_ϵ is a geometrical function and $\mathbf{H}$ is the extra body force that will be used to incorporate further details of the ESL and particulate effects, such as the RBC interface force density (pressure step) defined below. To solve governing Equations (19) and (20), we combine the LB methods of [50] with the model of [51], which allows for the introduction of two immiscible fluid components and the formation of interfaces embedding surface tension Laplace's law. The extended scheme developed here is completely Eulerian and represents a two-way coupled RBC and flow within a single framework. To complete the algorithm, we mention that, for multiple fluid, the propagation step is augmented by a fluid segregation process that ensures the correct kinematics and dynamics and good integrity for an interface between completely immiscible fluid components, representing RBC and plasma, as discussed above [51]. The propagation step is expressed as

$$R_p(\mathbf{x}+\mathbf{c}_p\Delta t, t+\Delta t) = \frac{R}{\rho} f_p^+ + w_p \beta \frac{RB}{\rho} \cdot \mathbf{c}_\mathrm{p} \cdot \mathbf{n}$$
$$B_p(\mathbf{x}+\mathbf{c}_p\Delta t, t+\Delta t) = \frac{B}{\rho} f_p^+ - w_p \beta \frac{RB}{\rho} \cdot \mathbf{c}_\mathrm{p} \cdot \mathbf{n} \tag{21}$$

where the density of each fluid component is given by $R = \sum_p R_p(\mathbf{x}, t)$ and $B = \sum_p B_p(\mathbf{x}, t)$, the combined particle distribution function is $f_p = R_p + B_p$ and f_p^+ accounts for the collided combined distribution. In Equation (21), β represents an interfacial segregation parameter and $\mathbf{n}$ the interfacial unit normal vector. We also note that, if only one fluid component exists, Equation (21) reduces to the standard LB propagation step (Equation (2)). The extended bi-component immiscible fluid model benefits from the interfacial kinematics and a near-complete absence of unphysical fluxes and spurious velocities. It can access the relevant biological regimes and retain the advantageous scaling of computational effort, as the number of droplets increases [52].

Returning to the definition of the extra body force term, $\mathbf{H}$ in Equation (20), which incorporates both particulate and glycocalyx forces, this is defined as

$$\mathbf{H} = \frac{\sigma}{2\rho} \pi \nabla \rho_N + \mathbf{E} \tag{22}$$

The left-hand side term imposes an interfacial tension σ on multicomponent particles. Here $\pi = \nabla \cdot \mathbf{n}$ is the local curvature and $\rho_N = (R - B)/(R + B)$ is a phase field indicator. The right-hand term $\mathbf{E}$ is a glycocalyx force that acts upon the particles as described in the following section.

In the proposed model of the ESL as a porous layer, the porosity is reduced by a compressive encounter with an erythrocyte. As a consequence, the ESL is squashed locally transporting the same mass into a smaller volume and consequently decreasing the porosity in that region. Even in the simplest situation, the ESL–lumen boundary should not be regarded as sharp, and there is an *uncertainty region* between bulk, lumen and glycocalyx material [49]. Let us define a variable porosity $\epsilon(\mathbf{x})$ that tends to 1 in the lumen region and gradually reduces, as it enters the glycocalyx region, where it approaches a minimum value, ϵ_G. This porosity transition is modelled through the increasing smooth function:

$$\epsilon(\mathbf{x}) = \epsilon_G + \frac{1-\epsilon_G}{2}[1 - \tan h\,(\xi(s-l))] \tag{23}$$

where l is the mean ESL thickness and the parameter $1/\xi$ determines the distribution of (i.e. the effective standard deviation of) protein chain lengths, while $s(\mathbf{x})$ denotes distance measured normally to the endothelial surface (Figure 7). Note that $\epsilon_G \leq \epsilon(\mathbf{x}) \leq 1$ and that for $\epsilon \to 1$, we have $\mathbf{F} \to \mathbf{H}$ (see Equation (20)), and Equations (19) and (20) reduce to the multi-component Navier–Stokes equations for free multi-component fluid flows. On the other hand, an additional, fictitious, repulsive body force density acts on the drop interface which enters the ESL region, impinging on the lumen. This force distribution is so designed that its accumulation produces an effective Hookean force acting at the centre of the local volume. Specifically, the erythrocyte is subjected to a surface force distribution, effective in the ESL only, which is directed everywhere in the drop-surface normal direction. This force device effectively models the glycocalyx as a continuum of elastic springs, with modulus E, gradually decaying from a maximum value, E_G (in the ESL) to 0 (towards the bulk):

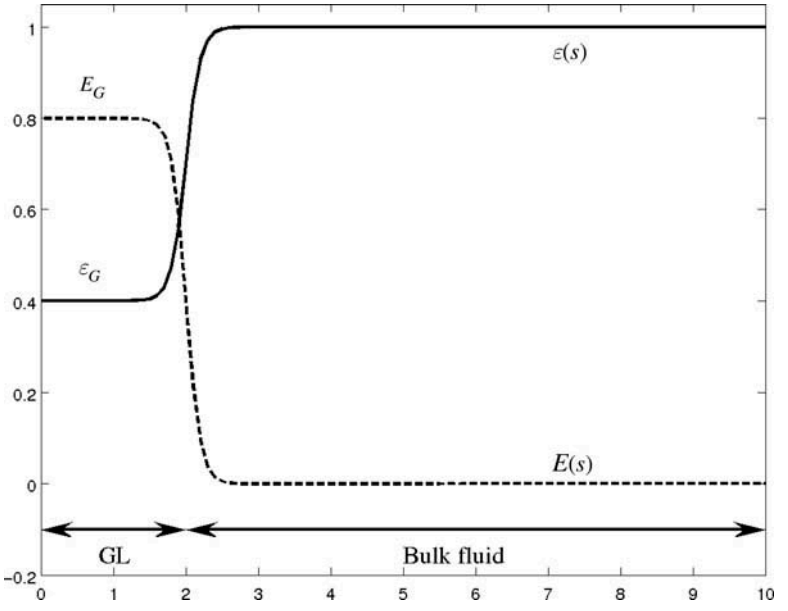

Figure 7. The porosity function ε (continuous line) as a function of the distance s: the latter increases form a minimum value ε_G (in the ESL or glycocalyx) to the bulk fluid ($\varepsilon = 1$). Similarly, the elasticity modulus E (dashed line) varies from a maximum value E_G in ESL to 0 (no elastic force) out of it. Note the smooth transition region (due to the uncertain ESL thickness) controlled by the parameter ξ.

$$E(\mathbf{x}) = \frac{E_G}{2}[1 - \tan h\,(\xi(s - l))] \tag{24}$$

where all notations are given in correspondence to Equation (23) (Figure 7).

It is important to note that the above force acts solely on the drop and not on the plasma. Hence, the relative density of the material which comprises the drop may be modelled by appropriate choice of the spring constant E_G in the above equation. A common difficulty in modelling low-scale physiological process is the identification of reliable estimates of the model parameters. Experiments in micro-haemodynamics are often prohibitively expensive or impossible *in vivo* and the only available source are data from literature. Due to their complex interplay between the fluid, the suspended bodies and the arterial wall, comprehensive models are difficult to be settled. Such models depend on so many variables and parameters that, if not appropriately simplified, they raise more questions than useful answers. Actually, we have chosen parameters which are in the correct range and where simulations provide results which are consistent with observation and experimental data. A number of simulations have been carried out in the case of an axi-symmetric channel having the same corrugation repeated along the length. Its size (of order of μm) is slightly larger than a single RBC flowing through it, driven by a constant pressure gradient with periodic conditions. At such fine scale, for accuracy purposes, the off-lattice non-slip endothelial surface uses continuous bounce-back conditions [27]. The ESL structure has been modelled as a porous layer of constant thickness over the undulated wall [52].

As one may expect, the average velocity of the drop is slower in the presence of glycocalyx, which constitutes a hindrance for the lumen flow. Also, the mean deformation

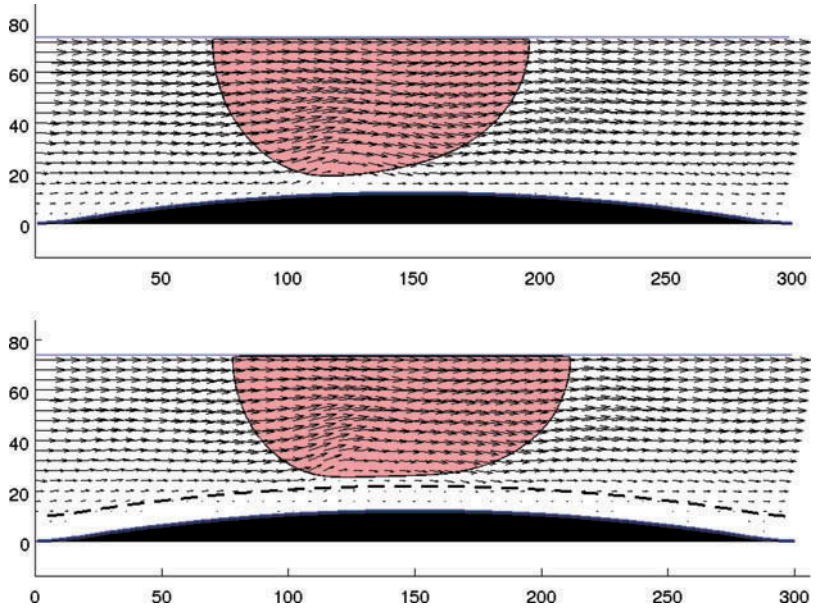

Figure 8. The velocity field for the particulate fluid in the region of the endothelium. The extent of the ESL is indicated by the broken line. An enhanced recirculation region is induced by the porous media (bottom), with respect to an experiment without glycocalyx (top). The single deformable drop has been acted on by encountering the glycocalyx body force field. The flow appears to be deflected up, which would tend to protect the endothelial surface from increased WSS.

of the drop is more pronounced with the glycocalyx force (Figure 8). Hence, when the drop is in the ESL influence region, it is subjected to the elastic force, which squeezes and lifts it away from the boundary, whilst making its shape more elongated. Considering the action of the glycocalyx as a sensor of mechanical forces, it is worth computing the shear stress at the glycocalyx/lumen boundary (GSS). Figure 9 shows the differences for WSS in the cases without and with glycocalyx: it evidences, in the latter case, a reduction of the shearing stress either at the wall (WSS, due to the plasma only) or at the ESL top (GSS, due to or the particulate fluid). It is possible that cilia, which deform preferentially at their tip, would be more likely to protect the EC from WSS fluctuations associated with RBCs transits [9].

As a comprehensive computational tool to account fov the different aspects of blood flow simulation in a unified LB framework, we developed the software MUPHY that involves five basic steps: (1) acquisition of MDCT data, (2) data segmentation into a stack of slices, (3) mesh generation from the segmented slices, (4) flow simulation and (5) data analysis and visualization. The MUPHY simulation package is designed to handle generic geometries, such as those provided by the MDCT acquisitions, and to run large-scale simulations on commodity or high-performance hardware resources. The major advantage of MUPHY is the possibility of concurrently simulating fluid dynamics together with suspended bodies at cellular and molecular scales. This multiscale methodology arises from the combined use of LB and molecular dynamics techniques [20].

For a 50 μm resolution of the vessels, which is sufficient to obtain well converged WSS distributions, the number of mesh points is easily in excess of 10^6. In these conditions, steady-state simulation requires $\simeq 5 \times 10^4$ timesteps, while pulsatile flows account for

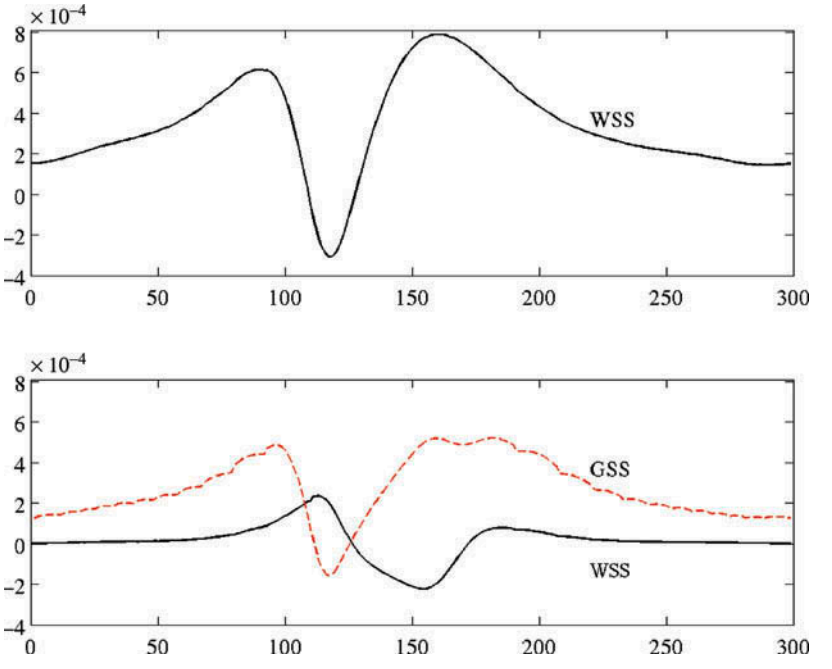

Figure 9. The WSS and GSS along the channel at the same time without (top) and with glycocalyx (bottom).

about 10^6 timesteps. The simulation of a pure LB is of the order of 0.06 sec/timestep on a serial run over a standard CPU. The computing time drops by orders of magnitude when employing graphical processing units (GPUs) or parallel simulations on multiple CPUs or GPUs, owing to the strong amenability of LB to parallel computing. By considering simulations at finite hoematocrit, the mesh resolution has to be increased with a mesh spacing below 20 μm, in order to resolve sufficiently the hydrodynamics of the RBCs. In this case, the simulation time increases by a factor of 20–50, as compared to the pure LB simulation. Therefore, massively parallel simulations on either CPUs or GPUs are required and given the excellent scalability of the simulations technique on both types of platforms, the study of entire coronary system becomes feasible [20,46].

6. Conclusions

Summarizing, it is shown that the LB method offers an extremely flexible and powerful framework to deal simultaneously with blood plasma, RBCs and glycocalyx in a unified and consistent form. The versatility of this framework configures a very appealing candidate for the computational study of biological fluids across scales of motion. More precisely, we have proposed a coarse-grained model of the blood flow over the exact, microscale, corrugated EC shape, covered by a prototype ESL, along with two-component immiscible fluid model. The model preserves the underlying simplicity of the LB algorithm; hence, all of its computational advantages, including its Eulerian nature, permits to do away with the laborious re-meshing procedures, typical of hybrid Lagrangian schemes. Restricted to idealized models for RBC dynamics, endothotelial corrugations and glycocalyx structures, the paper aims at showing that LB method provides an encompassing analytical and computational framework to embed different scales. The present study does

contain room for generalizations and is open to many directions for future research in CHD. The first step is to enhance our current, simplistic, interfacial tension model with additional stresses and bending properties associated with elastic structures. This would permit to model complex fluid-interface phenomena, such as tank-treading behaviour of the biological membrane coating the RBC.

If, at one hand, the microscopic blood–wall interaction has noticeable effects on pathological states, on the other hand, the accurate description of large-scale circulatory features relies on sophisticated pre-simulation imaging techniques and powerful simulation methods. In this respect, improved boundary conditions, especially at the outlet of the cardiovascular network, are in constant demand.

The unifying hydrokinetic methodology presented here has potential to accommodate both large-and small-scale aspects, thereby offering a reliable and robust approach to the understanding of cardiovascular disease in multiple-scale arterial systems, with great impact on physiological and biomedical applications.

Funding

The work was partially supported by the Italian MIUR-CNR project *InterOmics*, 2012–2013.

References

[1] V.L. Rayz and S.A. Berger, *Computational modeling of vascular hemodynamics*, Comput. Model. Biomech. 5 (2010), pp. 171–206.
[2] J. Zhang, P.C. Johnson, and A.S. Popel, *Effects of erytrocyte deformability and aggregation on the cell free layer and apparent viscosity of microscopic blood flows*, Microvasc. Res. 77 (3) (2009), pp. 265–272.
[3] Y.S. Chatzizisis, M. Jonas, A.U. Coskun, R. Beigel, B.V. Stone, C. Maynard, R.G. Gerrity, W. Daley, C. Rogers, E.R. Edelman, C.L. Feldman, and P.H. Stone, *Prediction of the localization of highrisk coronary atherosclerotic plaques on the basis of low endothelial shear stress: an intravascular ultrasound and histopathology natural history study*, Circulation 117 (8) (2008), pp. 993–1002.
[4] A.M. Shaaban and A.J. Duerinckx, *Wall shear stress and early atherosclerosis: a review*, AJR Am. J. Roentgenol. 174 (6) (2000), pp. 1657–1665.
[5] C.G. Caro, J.M. Fitzgerald, and R.C. Schroter, *Arterial wall shear stress and distribution of early atheroma in man*, Nature 223 (1969), pp. 1159–1161.
[6] A.M. Malek, S.L. Alper, and S. Izumo, *Hemodynamic shear stress and its role in atherosclerosis*, J. Am. Med. Assoc. 282 (21) (1999), pp. 2035–2042.
[7] D.A. Vorp, D.A. Steinman, and C.R. Ethier, *Computational modeling of arterial biomechanics*, Comput. Sci. Eng. 3 (2001), pp. 51–64.
[8] M.Y. Pahakis, J.R. Kosky, R.O. Dull, and J.M. Tarbell, *The role of endothelial glycocalyx components in mechanotransduction of fluid shear stress*, Biochem. Biophys. Res. Comm. 355 (1) (2007), pp. 228–233.
[9] G. Pontrelli, C.S. König, I. Halliday, T.J. Spencer, M.W. Collins, Q. Long, and S. Succi, *Modelling wall shear stress in small arteries using the Lattice Boltzmann method: influence of the endothelial wall profile*, Med. Eng. Phys. 33 (7) (2011), pp. 832–839.
[10] S. Weinbaum, J.M. Tarbell, and E.R. Damiano, *The structure and the function of the endothelial glycocalyx layer*, Ann. Rev. Biom. Eng. 9 (2007), pp. 121–167.
[11] T.W. Secomb, R. Hsu, and A.R. Pries, *Blood flow and red blood cell deformation in nonuniform capillaries: effects of the endothelial surface layer*, Microcirculation 9 (2002), pp. 189–196.
[12] N. Arlsan, *Mathematical solution of the flow field over glycocalyx inside vascular system*, Math. Comp. Appl. 12 (2007), pp. 173–179.
[13] P.E. Vincent, S.J. Sherwin, and P.D. Weinberg, *Viscous flow over outflow slits covered by an anisotropic Brinkman medium: a model of flow above interendothelial cell cleft*, Phys. Fluids 20 (6) (2008), p. 063106.
[14] F.J. Rybicki, H.J. Otero, M.L. Steigner, G. Vorobiof, L. Nallamshetty, D. Mitsouras, H. Ersoy, R.T. Mather, P.F. Judy, T. Cai, K. Coyner, K. Schultz, A.G. Whitmore, and M.F. Di Carli,

Initial evaluation of coronary images from 320-detector row computed tomography, Intl. J. Cardiovasc. Imaging 24 (5) (2008), pp. 535–546.

[15] D. Alemani, F. Pappalardo, M. Pennisi, S. Motta, and V. Brusic, *Combining cellular automata and lattice Boltzmann method to model multiscale avascular tumor growth coupled with nutrient diffusion and immune competition*, J. Immunol. Meth. 376 (2101), pp. 55–68.

[16] C. Bianca, *Thermostatted kinetic equations as models for complex systems in physics and life sciences*, Phys. Life Rev. 9 (2012), pp. 359–399.

[17] R. Ouared and B. Chopard, *Lattice Boltzmann simulations of blood flow: non-Newtonian rheology and clotting processes*, J. Stat. Phys. 121 (2005), pp. 209–221.

[18] D.J.W. Evans, P.V. Lawford, J. Gunn, D. Walker, D.R. Hose, R.H. Smallwood, B. Chopard, M. Krafczyk, J. Bernsdorf, and A. Hoekstra, *The application of multiscale modelling to the process of development and prevention of stenosis in a stented coronary artery*, Phil. Trans. R. Soc. A 366 (1879) (2008), pp. 3343–3360.

[19] S. Melchionna, M. Bernaschi, S. Succi, E. Kaxiras, F. J. Rybicki, D. Mitsouras, A. U. Coskun, and C. L. Feldman, *Hydrokinetic approach to large-scale cardiovascular blood flow*, Comput. Phys. Comm. 181 (2010), pp. 462–472.

[20] M. Bernaschi, S. Melchionna, S. Succi, M. Fyta, E. Kaxiras, and J.K. Sircar, *MUPHY: a parallel MULti PHYsics/scale code for high performance bio-fluidic simulations*, Comp. Phys. Comm. 180 (2009), pp. 1495–1502.

[21] S. Succi, *The Lattice Boltzmann Equation for Fluid Dynamics and Beyond*, Oxford University Press, Oxford, 2001.

[22] G. Pontrelli, S. Ubertini, and S. Succi, *The unstructured lattice Boltzmann method for non-Newtonian flows*, J. Stat. Mech. Theory & Exp. P06005 (2009).

[23] A. Caiazzo, D. Evans, J.L. Falcone, J. Hegewald, E. Lorenz, D. Stahl, B. Wang, J. Bernsdorf, B. Chopard, J. Gunn, R. Hose, M. Krafczyk, P. Lawford, R. Smallwood, D. Walker, and A. Hoekstra, *A complex automata approach for in-stent restenosis: two-dimensional multiscale modeling and simulations*, J. Comput. Sci. 17 (2) (2011), pp. 9–17.

[24] J. Boyd, J.M. Buick, and S. Green, *Analysis of the Casson and Carreau-Yasuda non-Newtonian models in steady and oscillatory flows using the lattice Boltzmann method*, Phys. Fluids 19 (2007), p. 032103.

[25] J. Janela, G. Pontrelli, A. Sequeira, S. Succi, and S. Ubertini, *Unstructured lattice-Boltzmann methods for hemodynamics flows with shear-dependent viscosity*, Int. J. Modern Phys. 21 (6) (2010), pp. 1–17.

[26] R. Benzi, S. Succi, and M. Vergassola, *Theory and application of the lattice Boltzmann equation*, Phys. Rep. 222 (3) (1992), p. 147.

[27] M. Bouzidi, M. Firdaouss, and P. Lallemand, *Momentum transfer of a Boltzmann-lattice fluid with boundaries*, Phys. Fluids 13 (11) (2001), pp. 3452–3459.

[28] A.J.C. Ladd and R. Verberg, *Lattice-Boltzmann simulations of particle-fluid suspensions*, J. Stat. Phys. 104 (5) (2001), pp. 1191–1251.

[29] Z. Guo, C. Zheng, and B. Shi, *An extrapolation method for boundary conditions in lattice Boltzmann method*, Phys. Fluids 14 (2002), p. 2007.

[30] J. Boyd and J.M. Buick, *Three-dimensional modelling of the human carotid artery using the lattice Boltzmann method: II. Shear analysis*, Phys. Med. Biol. 53 (20) (2008), pp. 5781–5795.

[31] T. Krüger, F. Varnik, and D. Raabe, *Shear stress in lattice Boltzmann simulations*, Phys. Rev. E 79 (2009), p. 036304.

[32] M. Junk, *A finite difference interpretation of the lattice Boltzmann method*, Num. Meth. Partial Diff. Equ. 17 (4) (2001), pp. 383–402.

[33] B. Stahl, B. Chopard, and J. Latt, *Measurements of wall shear stress with the lattice Boltzmann method and staircase approximation of boundaries*, Comp. Fluids 39 (4) (2010), pp. 1625–1633.

[34] S. Melchionna, E. Kaxiras, M. Bernaschi, and S. Succi, *Endothelial shear stress from large-scale blood flow simulations*, Phil. Trans. R. Soc. A: Math. Phys. Eng. Sci. 369 (1944) (2011), pp. 2354–2361.

[35] T.F. Sherman, *On connecting large vessels to small. The meaning of Murray's law*, J. Gen. Physiol. 78 (4) (1981), pp. 431–453.

[36] Q. Zou and X. He, *On pressure and velocity boundary conditions for the lattice Boltzmann BGK model*, Phys. Fluids 9 (6) (1997), p. 1591.

[37] J. Latt, B. Chopard, O. Malaspinas, M. Deville, and A. Michler, *Straight velocity boundaries in the lattice Boltzmann method*, Phys. Rev. E 77 (5) (2008), p. 056703.
[38] M. Junk and Z. Yang, *Asymptotic analysis of lattice Boltzmann outflow treatments*, Commun. Comput. Phys. 9 (5) (2011), pp. 1117–1127.
[39] S. Melchionna, *A model for red blood cells in simulations of large-scale blood flows*, Macromol. Theory & Sim. 20 (2011), p. 548.
[40] J.F. Brady and G. Bossis, *Stokesian dynamics*, Ann. Rev. Fluid Mech. 20 (1988), p. 111.
[41] Z.L. Guo, C.G. Zheng, and B.C. Shi, *Discrete lattice effects on the forcing term in the lattice Boltzmann method*, Phys. Rev. E 65 (11) (2002), p. 046308.
[42] J.G. Gay and B.J. Berne, *Modification of the overlap potential to mimic a linear site–site potential*, J. Chem. Phys. 74 (1981), p. 3316.
[43] M.P. Allen and G. Germano, *Expressions for forces and torques in molecular simulations using rigid bodies*, Mol. Phys. 104 (2006), p. 3225.
[44] S. Melchionna, *Design of quasisymplectic propagators for Langevin dynamics*, J. Chem. Phys. 127 (2007), p. 044108.
[45] A. Dullweber, B. Leimkuhler, and R. Mclachlan, *A symplectic splitting method for rigid-body molecular dynamics*, J. Chem. Phys. 107 (1997), p. 5851.
[46] S. Melchionna, G. Amati, M. Bernaschi, M. Bisson, S. Succi, D. Mitsouras, and F.J. Rybicki, *Risk assessment of atherosclerotic plaques based on global biomechanics*, Med. Eng. Phys. 35 (9) (2013), pp. 1290–1297.
[47] T. Reichlin, A. Wild, M. Dürrenberger, A.U. Daniels, U. Aebi, P.R. Hunziker, and M. Stolz, *Investigating native coronary artery endothelium in situ and in cell culture by scanning force microscopy*, J. Struct. Biol. 152 (2005), pp. 52–63.
[48] S. Ubertini and S. Succi, *Recent advances of lattice Boltzmann techniques on unstructured grids*, Prog. Comput. Fluid Dyn. 5 (1/2) (2005), pp. 84–96, PMID: 1870131.
[49] G. Pontrelli, I. Halliday, T.J. Spencer, C.M. Care, C.S. König, and M.W. Collins, *Near wall hemodynamics: modelling the glycocalyx and the endothelium surface*, Proceedings Micro and Nano Flows Conference, MNF2011, Thessaloniki, 22–24 August 2011.
[50] Z. Guo and T.S. Zhao, *Lattice Boltzmann model for incompressible flows through porous media*, Phys. Rev. E 66 (2002), p. 036304.
[51] I. Halliday, A.P. Hollis, and C.M. Care, *Lattice Boltzmann algorithm for continuum multicomponent flow*, Phys. Rev. E 76 (2007), p. 026708.
[52] G. Pontrelli, I. Halliday, T.J. Spencer, C.S. König, and M.W. Collins, *Modelling the glycocalyx-endothelium-erythrocyte interaction in the microcirculation: a computational study*, Comp. Meth. Biomech. Biomed. Eng. (2013), Published online. doi:10.1080/10255842.2013.799146.